On the transition of the cylinder wake

Hong-Quan Zhang,[a),b)] Uwe Fey, and Bernd R. Noack,[a)]
Max-Planck-Institut für Strömungsforschung, Bunsenstrasse 10, D-37073 Göttingen, Germany

Michael König and Helmut Eckelmann
Institut für Angewandte Mechanik und Strömungsphysik der Universität, Bunsenstrasse 10, D-37073 Göttingen, Germany

(Received 9 March 1994; accepted 8 December 1994)

The transition of the cylinder wake is investigated experimentally in a water channel and is computed numerically using a finite-difference scheme. Four physically different instabilities are observed: a local "vortex-adhesion mode," and three near-wake instabilities, which are associated with three different spanwise wavelengths of approximately 1, 2, and 4 diam. All four instability processes can originate in a narrow Reynolds-number interval between 160 and 230, and may give rise to different transition scenarios. Thus, Williamson's [Phys. Fluids **31**, 3165 (1988)] experimental observation of a hard transition is for the first time numerically reproduced, and is found to be induced by the vortex-adhesion mode. Without vortex adhesion, a soft onset of three-dimensionality is numerically and experimentally obtained. A control-wire technique is proposed, which suppresses transition up to a Reynolds number of 230. © *1995 American Institute of Physics.*

I. INTRODUCTION

The incompressible flow around a circular cylinder represents one of the most investigated prototypes of bluff-body wakes. The properties of this flow depend on the Reynolds number $\mathrm{Re}=UD/\nu$, where U is the velocity of the oncoming flow, D is the diameter of the cylinder, and ν is the kinematic viscosity of the fluid. Most authors agree that the transition scenario contains a two-dimensional (2-D) instability from a 2-D steady to a 2-D periodic wake at $\mathrm{Re}_{c1}\approx 45$ and a three-dimensional (3-D) transition at a Reynolds number Re_{c2} between 150 and 210. While the onset of periodicity has been conclusively identified as a supercritical Hopf bifurcation,[1–3] there still exist many contradictory results regarding the onset of three-dimensionality. Williamson[4,5] experimentally observes a hard hysteretical transition towards an irregular wake, accompanied with a jump of the Strouhal number $\mathrm{St}=fD/U$ (f: dominant frequency) and the base pressure[6] at the transition Reynolds number 180. The jump of the Strouhal number is also confirmed for different cylinder end conditions by König, Noack, and Eckelmann[7] and by Brede *et al.*[8] In contrast, seemingly all recent 3-D numerical simulations of Karniadakis and Triantafyllou,[9] Tomboulides, Triantafyllou, and Karniadakis,[10] and Noack and Eckelmann[11,12] indicate a soft transition to a 3-D, periodic flow.

Recent values for the critical Reynolds number Re_{c2} range from 150 to 210 in the cited references. Most authors report that the 3-D wake at $\mathrm{Re}\approx\mathrm{Re}_{c2}$ is characterized by a wake pattern with a dominant spanwise wavelength, $\lambda_{z,c2}$. The reported values for this wavelength lie between 1–4 diam.[13–16] While Williamson observes a transition from large spanwise patterns with a wavelength $\lambda_z\approx 3D$ (his *A mode*) to a fine-scale pattern with a size of $1D$ (his *B mode*) near $\mathrm{Re}\approx 230$, the global stability analysis of Noack and Eckelmann yields an intermediate value of $1.8D$. Gerrard[17] emphasizes that also wavelengths of ten and more diameters can be found in some experimental works. Yet, these large structures seem to be induced by the strong perturbations at the experimental end conditions and have not been reproduced in more recent works with improved experimental facilities.

In addition to the wake patterns with a dominant spanwise wavelength, also localized vortex deformations, Williamson's[14] "vortex dislocations," are experimentally observed at transitional Reynolds numbers. At these "dislocations," the von Kármán vortices seem to "adhere" at a steady or slowly moving point at the cylinder for many periods. Hence, the *vortex-adhesion mode* may be a more suitable term for this phenomenon. Since there seems to exist no published numerical simulations of the vortex-adhesion mode, it cannot be conclusively settled whether these structures are only end effects due to the finite aspect ratio or if vortex adhesion may also be a self-sustaining shedding state for an infinitely long cylinder. While the vortex-adhesion phenomenon has been shown to have a large effect on the far wake,[14] their influence on the onset of three-dimensionality in the near wake is not well investigated so far. A further complication of the cylinder wake transition is the experimental observation that the far-wake structures and dominating time scales are less organized and significantly larger than the near-wake features.[18,19]

In the present publication, the cylinder wake transition is investigated in order to elucidate the reasons for the discrepancies in the literature. For this purpose, an accurate 3-D finite-difference scheme was developed[20] and a water channel was constructed.[21] In Sec. II, the construction and validation of the employed Navier–Stokes solver are described. In Sec. III, the experimental setup is outlined. The numerical and experimental results on the cylinder wake transition are

[a)]Also at the Deutsche Forschungsanstalt für Luft- und Raumfahrt, Institut für Strömungsmechanik, Bunsenstrasse 10, D-37073 Göttingen, Germany.
[b)]Permanent address: Department of Mechanics, Tianjin University, Tianjin 300072, People's Republic of China.

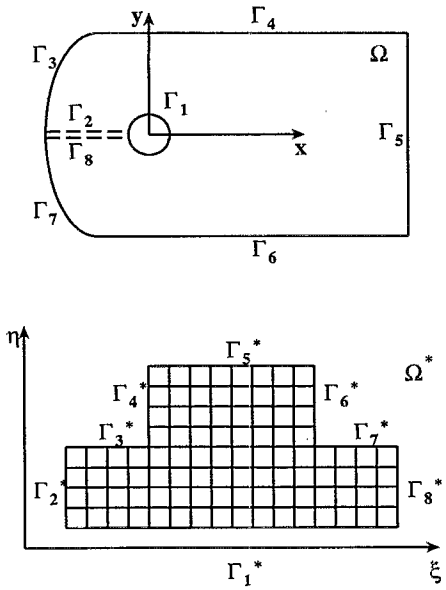

FIG. 1. Physical (top) and computational (bottom) domain for the finite-difference scheme.

detailed in Sec. IV. Finally (Sec. V), the main findings are summarized and discussed.

II. NUMERICAL METHOD

In this section, the incompressible Navier–Stokes solver is described. This solver is based on a finite-difference method for generalized coordinates on a boundary-fitted grid.[22] First (Sec. II A), the generation of the grid is outlined. In Sec. II B, the finite-difference scheme and the employed boundary conditions are discussed. Finally (Sec. II C), the numerical scheme is validated for 2-D and 3-D solutions.

A. Grid generation

In the following, the flow is described in a Cartesian coordinate system x,y,z, where the x axis is aligned with the oncoming flow, the z axis coincides with the axis of symmetry of the cylinder, and the y axis is perpendicular to the x and z directions. These coordinates are assumed to be nondimensionalized with the cylinder diam D, i.e., the cylinder surface is described by $\sqrt{x^2+y^2} = \frac{1}{2}12$.

The numerically resolved physical domain in the x,y plane consists of a half-ellipse in the front joined by a rectangle for the wake region (see Fig. 1, top). This domain is similar to the one used by Karniadakis and Triantafyllou[23,9] for 2-D and 3-D cylinder wake simulations, except that they use a half-circle in the upstream region. Following the work of Thompson *et al.*, the physical domain is mapped on a simpler T-shaped computational domain (see Fig. 1, bottom). The cylinder is mapped onto the line Γ_1^*, the outflow boundary onto Γ_5^*, the upper and lower boundaries of the wake rectangle onto Γ_4^* and Γ_6^*, respectively, and the upstream half-ellipse onto Γ_3^* and Γ_7^*. The boundaries Γ_2^* and Γ_8^* denote the cut $y=0$ in the front region. The computational domain is described by an orthogonal coordinate system ξ,η. In this system, all boundaries of the physical domain coincide with coordinate lines ξ=const or η=const. The dimensions of the ξ and η coordinates are chosen so that the partition of the grid consists of unit squares, i.e., the ξ and η coordinates of the grid lines are integers.

Following Thompson *et al.*,[22] the mapping $x=x(\xi,\eta)$, $y=y(\xi,\eta)$ from the computational to the physical domain is obtained by numerically solving the following system of Poisson equations with Dirichlet boundary conditions:

$$\alpha \frac{\partial^2 x}{\partial \xi^2} - 2\beta \frac{\partial^2 x}{\partial \xi\, \partial \eta} + \gamma \frac{\partial^2 x}{\partial \eta^2} = -J^2\left(P \frac{\partial x}{\partial \xi} + Q \frac{\partial x}{\partial \eta}\right),$$

$$\alpha \frac{\partial^2 y}{\partial \xi^2} - 2\beta \frac{\partial^2 y}{\partial \xi\, \partial \eta} + \gamma \frac{\partial^2 y}{\partial \eta^2} = -J^2\left(P \frac{\partial y}{\partial \xi} + Q \frac{\partial y}{\partial \eta}\right),$$

where $\alpha=\partial^2 x/\partial\eta^2+\partial^2 y/\partial\eta^2$, $\beta=(\partial x/\partial\xi)(\partial x/\partial\eta)+(\partial y/\partial\xi)(\partial y/\partial\eta)$, $\gamma=\partial^2 x/\partial\xi^2+\partial^2 y/\partial\xi^2$, and $J=\partial(x,y)/\partial(\xi,\eta)=(\partial x/\partial\xi)(\partial y/\partial\eta)-(\partial x/\partial\eta)(\partial y/\partial\xi)$. With the source functions $P(\xi,\eta)$ and $Q(\xi,\eta)$, the density of grid lines in the physical domain can be increased or decreased in regions with large or small gradients (see, e.g., Chap. 13 of Fletcher[24]). In the present publication, $P=0$ and $Q=a_l \exp(-c_l\eta)$, where coefficients a_l and c_l are chosen in order to increase the radial resolution close to the cylinder surface. In the wake region, the source terms vanish and the mapping $(\xi;\eta)\mapsto(x;y)$ becomes locally orthonormal.

The size of a 2-D computational domain around the cylinder is described by three parameters; the size of the upstream region X_i, the x coordinate of the outflow boundary X_0, and the width of the wake rectangle Y_w. The inflow boundary is a half-ellipse with a principal axis ratio of 1:2. The numerically resolved physical domain is therefore bounded by $-X_i<x<X_0$ and $|y|<Y_w/2$ (see Fig. 2, bottom). The grid C, illustrated in Fig. 2 (bottom), is employed for the numerical computations. For validation purposes, two other grids with either smaller dimensions (grid A) or larger grid spacings (grid B) are generated (see Fig. 2, top and middle). The geometric parameters and the resolution of the grids are displayed in Table I. Here, N_ξ and N_η represent the number of grid points in the ξ and η directions. Here Δx_0 and Δy_0 are the grid spacings in the x and y directions, respectively, near the outflow boundary. Also, Δs_n denotes the grid spacing on the cylinder surface in the normal direction.

Since the computation is effected in the computational domain, the Navier–Stokes equations have to be expressed in terms of the coordinates ξ,η. The transformation of the spatial derivatives in the physical domain read as

$$\frac{\partial}{\partial x} = \frac{1}{J}\left(y_\eta \frac{\partial}{\partial \xi} - y_\xi \frac{\partial}{\partial \eta}\right),$$

$$\frac{\partial}{\partial y} = \frac{1}{J}\left(-x_\eta \frac{\partial}{\partial \xi} + x_\xi \frac{\partial}{\partial \eta}\right), \quad \text{etc.}$$

Further details can be inferred from most textbooks of computational fluid dynamics, for instance, from Chap. 13 of Fletcher.[24]

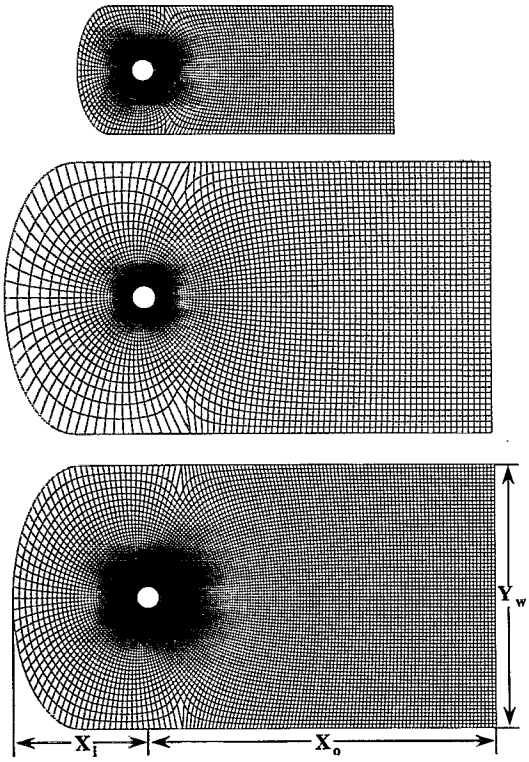

FIG. 2. Grids A, B, and C (top to bottom).

B. Finite-difference scheme

The velocity field in terms of the location $\mathbf{x}=(x;y;z)$ and the time t is described by $\mathbf{u}=(u;v;w)$, where u, v, and w are the components in x, y, and z directions. The pressure is denoted by p. In the following, all independent and dependent variables are assumed to be nondimensionalized with the diam D and the velocity of the oncoming flow U. The evolution of the incompressible velocity field is described by the Navier–Stokes and the continuity equations,

$$\frac{\partial \mathbf{u}}{\partial t}+(\mathbf{u}\cdot\nabla)\mathbf{u}=-\nabla p+\frac{1}{\mathrm{Re}}\nabla^2\mathbf{u},$$

$$\nabla\cdot\mathbf{u}=0.$$

For the numerical computations, the boundary conditions cannot be imposed at infinity, but have to be specified at the boundary of the numerically resolved physical domain. At the cylinder surface, the no-slip condition $\mathbf{u}=0$ is enforced. The normal pressure gradient is set equal to zero, i.e., a homogeneous von Neumann condition is imposed on p. The exact condition may be derived from the Navier–Stokes equations. Yet, this condition converges to the von Neumann condition in the boundary-layer approximation at large Reynolds numbers and is numerically found to yield insignificantly different solutions. At the inflow boundary, the velocity and the pressure are assumed to be uniform, $\mathbf{u}=(U;0;0)$ and $p=\text{const}$. At the sides of the wake rectangle $y=\pm Y_w/2$, vanishing normal gradients for all flow variables are assumed, i.e., $\partial\mathbf{u}/\partial y=\partial p/\partial y=0$. The outflow boundary condition at $x=X_0$ should allow the vortices to leave without causing upstream perturbations. This is achieved by requiring vanishing third-order x derivatives, i.e., $\partial^3\mathbf{u}/\partial x^3=\partial^3 p/\partial x^3=0$. In the spanwise direction, the flow is assumed to be periodic with wavelength L.

The initial condition for a 2-D computation $(u;v;w)=(1;0;0)$ corresponds to an impulsive start. Asymmetric 2-D solutions may be obtained by adding a small perturbation to the uniform initial condition. Post-transient 2-D solutions superimposed by a 3-D perturbation are typically used as initial conditions for the 3-D computation. In a Reynolds number range of 160–230, small 3-D perturbations result in a smooth onset of three-dimensionality, whereupon large localized 3-D perturbations give rise to a hard hysteretical transition for a sufficiently large spanwise domain size L (see Sec. IV).

For 2-D computations, the velocity $\mathbf{u}$ at the node $(\xi;\eta)=(i;j)$ and the time level n is denoted by $\mathbf{u}_{ij}^n$. The velocity is expanded as a Taylor series in terms of the time,

$$\mathbf{u}_{ij}^{n+1}=\mathbf{u}_{ij}^n+\sum_{m=1}^{\infty}\frac{\Delta t^m}{m!}\left.\frac{\partial^m\mathbf{u}}{\partial t^m}\right|_{ij}^n.$$

The temporal order of a finite-difference method depends on the number of the considered terms in the truncated expansion. Methods with a temporal order larger than unity contain higher-order spatial derivatives that are not present in the original Navier–Stokes equations.[25] The implementation of these additional terms may make the scheme less economical, and also less accurate if the new terms are not treated properly. The time step Δt depends on the grid spacing, which must be small enough for the resolution of the velocity gradients, particularly near the cylinder surface. In the present publication, the chosen time step Δt varies from 10^{-2} to 10^{-3}. If only the first term in the temporal expansion is taken, the truncation error is insignificant,

$$\mathbf{u}_{ij}^{n+1}=\mathbf{u}_{ij}^n+\Delta t\left.\frac{\partial\mathbf{u}}{\partial t}\right|_{ij}^n+O(\Delta t^2).$$

For the temporal integration, a MAC-type finite-difference scheme (see, for instance, Chap. 17 in Fletcher[24]) is employed. In this scheme, the iteration is carried out in two steps on a staggered grid, where the pressure nodes and the velocity nodes are displaced by half a grid spacing. In the first step an intermediate velocity $\mathbf{u}^*$ is computed from the flow variables at time level n, according to

$$\mathbf{u}_{ij}^*=\mathbf{u}_{ij}^n+\Delta t\left.\left((\mathbf{u}\cdot\nabla)\mathbf{u}+\frac{1}{\mathrm{Re}}\nabla^2\mathbf{u}\right)\right|_{ij}^n. \tag{1}$$

TABLE I. Parameters of the grids used for the 2-D validation.

Grid	X_i	X_0	Y_w	$N_\xi\times N_\eta$	$\Delta x_0=\Delta y_0$	Δs_n	a_l	c_l
A	3.0	11.5	6.0	96× 96	0.1667	0.010	1000.0	0.3
B	6.0	16.0	12.0	102× 90	0.2500	0.012	1000.0	0.3
C	6.0	16.0	12.0	144×144	0.1667	0.008	1000.0	0.2

TABLE II. Strouhal number St, mean drag coefficient C_D, and RMS amplitude of the lift coefficient C_L' at Re=100 for 2-D grids A, B, and C.

Grid	St	C_D	C_L'
A	0.190	1.548	0.225
B	0.172	1.421	0.247
C	0.173	1.425	0.250

The RHS of Eq. (1) represents the discretization of the spatial derivatives at the node $(i;j)$ and the time level n. In the second step, the velocity is calculated for time level $n+1$:

$$\mathbf{u}_{ij}^{n+1}=\mathbf{u}_{ij}^{*}-\Delta t\ \nabla p|_{ij}^{*}. \tag{2}$$

Before the second step (2), the Poisson equation for pressure p,

$$\nabla^2 p|_{ij}^{*}=\frac{\nabla\cdot\mathbf{u}^{*}}{\Delta t},$$

is solved. While the intermediate field $\mathbf{u}^*$ is generally not solenoidal, the velocity field at time level $n+1$ can be shown to fulfill the discretized incompressibility condition.

The first-order spatial derivatives in the convective term of the Navier–Stokes equations are upwind discretized using four grid points (for details see Ref. 20). The second-order derivatives in the diffusion term are approximated by three-point central differences. Thus, a third-order upwind scheme is obtained, which is known to prevent nonphysical oscillation and which is expected to have negligible numerical viscosity on the employed boundary-fitted grid.

C. Validation

In order to study the effect of the domain size and the grid resolution on the 2-D solutions for the cylinder wake, computations are performed at Re=100 on three different grids (A, B, C). At this Reynolds number, 2-D parallel vortex shedding can be achieved in the laboratory with a careful treatment of the end conditions (Eisenlohr and Eckelmann[26]). Therefore, the influence of domain size and grid resolution can be assessed by investigating the discrepancy between the experimental and numerical Strouhal number values. The computed Strouhal numbers, mean drag coefficients, and RMS amplitudes of the lift coefficients are enumerated in Table II. The experimental Strouhal number at Re=100 is 0.167 using the empirical formula of König, Noack, and Eckelmann.[7] From Table II the numerical values for the Strouhal numbers are seen to be larger than the experimental value. The discrepancy is around 3% for grids B and C and about 12% for the smaller grid A. The improved grid resolution of grid C—as compared to grid B—seems to have little effect on the solution. In contrast, the numerical data for the Strouhal number appear to converge rapidly to the experimental value with increasing domain size. A similar tendency is reported by Karniadakis and Triantafyllou[9] for their cylinder wake simulation with a spectral method.

The performance of the finite-difference method in terms of the Reynolds numbers is investigated for the 2-D wake in the range 40<Re<300. For this computation grid C is employed. In Fig. 3 (top), the solid circles represent the computed Strouhal numbers. The curve is based on the empirical formula of König *et al.*[7] In the whole Reynolds number interval the computed values are about 3% larger than the experimental results. For an increased size of the computational domain, a smaller discrepancy is expected.

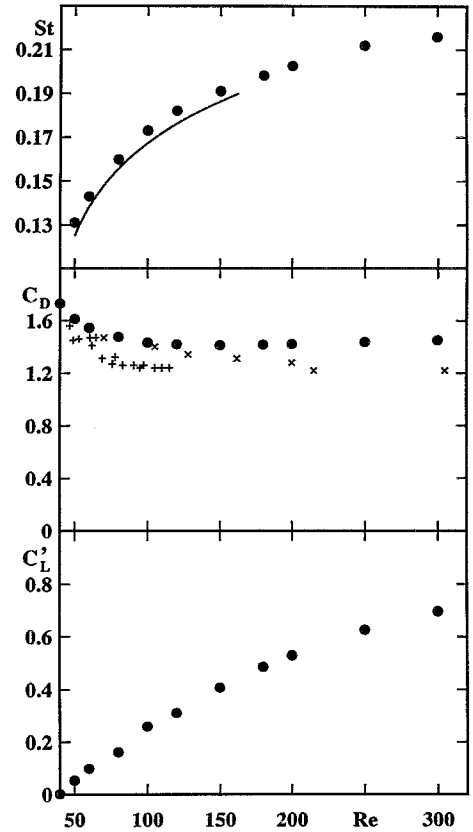

FIG. 3. Strouhal number St (top), mean drag coefficient C_D (middle), and RMS amplitude of the lift coefficient C_L' (bottom) in terms of the Reynolds numbers Re. The solid circles (●) denote our numerical values. The solid St vs Re curve represents the empirical formula of König *et al.*[7] for 2-D shedding. The symbols (+) and (×) refer to C_D measurements of Tritton[37] and Wieselsberger,[38] respectively.

The mean drag coefficient C_D and the RMS amplitude of the lift coefficient C_L' are presented in Fig. 3 (middle and bottom) in terms of the Reynolds number. The mean drag coefficients obtained in the 2-D computation are up to 20% larger at Re=300 than the experimental ones, since in the laboratory the flow is superimposed by 3-D fluctuations after the transition. For the lift coefficients, no experimental data has been found at low Reynolds numbers.

In the present work, also the influence of different outflow boundary conditions on the numerical results is investigated. The flow state is not noticeably changed, when the first, second, or the third downstream derivatives of flow variables are set equal to zero, except for minor differences near the outflow boundary.

In 3-D computations the numerical solution is affected by the spanwise domain size L and the spanwise grid spacing Δz—in addition to the 2-D grid. Therefore, the performance of the finite-difference scheme is studied for the different

TABLE III. Parameters of the grids used for the 3-D validation.

No.	Grid	Δz	L
1	A	0.1	3
2	B	0.1	3
3	C	0.1	3
4	C	0.1	6
5	C	0.1	9
6	C	0.05	3
7	C	0.2	3

2-D grids A, B, and C and various spanwise resolutions and domain sizes. In Table III, the parameters of the employed 3-D grids are listed. The first three entries #1, #2, and #3 in Table III correspond to grids A, B, and C with the same spanwise spacing $\Delta z=0.1D$ and the same spanwise dimension $L=3D$. In the 3-D grids, #3, #4, and #5, the spanwise wavelength is varied: $L=3D$, $6D$, and $9D$, using grid C and the same spanwise resolution $\Delta z=0.1D$. In the cases #3, #6, and #7, the spanwise resolutions are $\Delta z=0.1D$, $0.05D$, and $0.2D$, respectively, while the 2-D grid and spanwise dimension remain the same.

Table IV lists the corresponding numerical results for the developed 3-D solution, including Strouhal numbers, mean drag coefficients, RMS amplitudes of the lift coefficients, and RMS and maximum values of the spanwise velocity w averaged along a line parallel to the z axis for $x/D=1.5$ and $y=0$. The values for w_{RMS} and $w_{\max}$ can be viewed as amplitudes of three-dimensionality, since they vanish for 2-D flow. The Reynolds number chosen for this validation is 300, at which experiments show that the 3-D wake is dominated by fine-scale structures with a spanwise wavelength of about $1D$.[27] Using 3-D grid #1 with the smallest 2-D domain, the St and C_D values are significantly larger than for the other grids (see Table IV). For grid #2 with the coarse discretization of the x,y plane and for grid #7 with a coarse spanwise resolution, w_{RMS} and $w_{\max}$ are significantly smaller than that of finer grids, indicating that the 3-D instability processes seem to be insufficiently resolved.

Therefore, we use grid C as the x,y projection for the 3-D computations. Thus, reasonably accurate 2-D solutions and a good resolution of the 3-D fluctuations in the x,y plane are guaranteed. A spanwise grid spacing of $\Delta z=0.1D$ appears to be fine enough to resolve the small secondary vortex structures with spanwise wavelengths around $1D$. For 3-D structures of much larger wavelength, a slightly larger spanwise spacing of $0.15D$ is used for economical reasons.

TABLE IV. Strouhal number St, mean drag coefficient C_D, RMS amplitude of the lift coefficient C_L', RMS and maximum value of the spanwise velocity component, w_{RMS} and $w_{\max}$, at Re=300 for the 3-D grids, listed in Table III. The statistics of the spanwise velocity component are spatiotemporal averages with respect to the time and the z coordinate for $x/D=1.5$ and $y=0$.

No.	St	C_D	C_L'	w_{RMS}	$w_{\max}$
1	0.232	1.432	0.4217	0.0828	0.3376
2	0.210	1.292	0.4470	0.0667	0.2827
3	0.212	1.311	0.4507	0.0854	0.3637
4	0.212	1.278	0.4387	0.0886	0.3725
5	0.212	1.260	0.4298	0.0895	0.3736
6	0.212	1.308	0.4513	0.0901	0.3764
7	0.212	1.312	0.4506	0.0683	0.2984

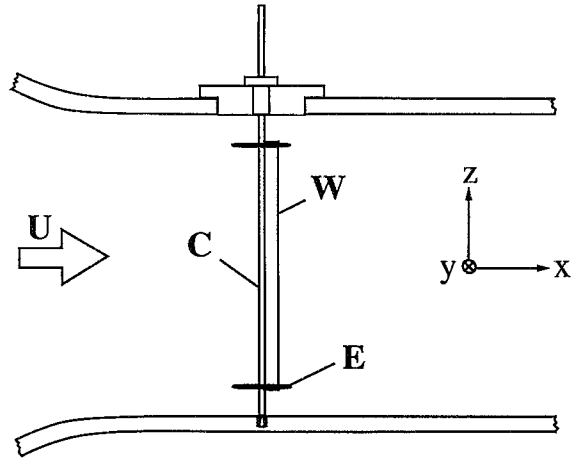

FIG. 4. Principal sketch of the test section. The cylinder C is mounted vertically. The hydrogen-bubble wire W is mounted at the end plates E.

III. EXPERIMENTAL SETUP

The experiments have been carried out in a water channel. A hydrogen-bubble method is applied to obtain a visual image of the cylinder wake. The channel is especially optimized for investigations at free-stream velocities between 3 and 15 cm/s. The honeycomb and various screens are modified so that a stationary, uniform velocity profile is achieved in the test section, which is 250 mm wide and 330 mm high. A detailed description of the channel is given by Fey.[21] Here, only the main features will be summarized.

The visualizations of the cylinder wake are carried out in the test section just behind the 4:1 contraction of the nozzle (Fig. 4). The cylinders have a polished surface and are made from stainless steel. Their diameters are 2, 3, and 4 mm, the corresponding aspect ratios and end conditions are listed in Table V. Thus, the transition range ($180<\mathrm{Re}<300$) is covered by the above velocity range, for which the channel is optimized. The cylinders are mounted vertically in the test section and are bounded by end plates or end cylinders in order to minimize end effects.

A 25 μm diam platinum–iridium wire is located at different positions in the test section and serves as the hydrogen-bubble wire. This wire is fixed directly at the confining end plates or at the end cylinders (see Fig. 4). By rotating the cylinder around its axis, the bubble wire can be located in different angular positions with respect to the front

TABLE V. Employed experimental setups.

No.	D (mm)	L/D	End conditions
1	2	133	End plates
2	3	50	End cylinders
3	3	93	End plates
4	4	71	End plates

stagnation point of the cylinder. Thus, the hydrogen bubbles can be introduced in different sheets of the separating shear layers. In the transition range, the location of the hydrogen-bubble wire proves to be an important parameter for the structures that can be observed in the cylinder wake. *In some locations, the visualization wire can have the effect of a control wire, the presence of which may drastically change the wake features.* In another configuration, the effect of the visualization wire on the wake features is avoided by placing it 15 cylinder diameters upstream and slightly offset from the plane $y=0$. In the present investigation, this configuration is employed for reasons of comparison. This aspect is discussed in detail in the following sections.

The Reynolds number of the hydrogen-bubble wire is of the order of unity in the present experiments. Hence, this wire cannot give rise to vortex shedding. A hydroelastic coupling of this wire with the vortex street behind the cylinder cannot *a priori* be excluded and is carefully examined. Typically, vibrations are easily observed by eyesight, since the characteristic frequency of the vortex shedding is only a few Hertz. For a more precise detection of possible wire vibrations, a nearly unidirectional light source is used. This light source is directed on the visualization wire at a small angle and a photodiode is located in the light ray reflected from the wire. Thus, small vibrations of the wire are indicated by the photodiode device. Hardly noticeable oscillations of the wire are only detected for a position near $(x_w/D;y_w/D)\approx(1,0)$. This setup corresponds to the retarded onset of three-dimensionality described in Sec. IV E. The wire remains steady for all other investigated positions in the whole regular and transitional Reynolds number range.

Images of the wake flow in the x,z plane are recorded by a CCD camera connected to a videotape recorder and a digital image processing system controlled by an IBM-compatible PC. Before each experiment, the velocity in the test section is determined optically. A hydrogen-bubble wire is fixed between the upper and lower tunnel walls at $x=-60$ mm, $y=-66$ mm and is pulsed to generate vertical time lines in the test section. At this location, the wire is inside the core region of the test section and has no noticeable influence on the cylinder wake. The velocity is determined from the time interval between two pulses and the distance of the corresponding time lines. This method proved to be of high accuracy and reproducibility.

The characteristic spanwise wavelength is measured manually from digitized images of the CCD camera. First, the x,z view section of the camera is determined by reference marks. Then, the camera records several hundred shedding periods. After an evaluation of the video, selected pictures are digitized and employed for measuring the length of the spanwise structures.

IV. PHENOMENOLOGY OF THE CYLINDER WAKE

In this section, numerical and experimental evidence for four distinct 3-D instability processes, which give rise to different transition scenarios, are presented. In Secs. IV A and IV B, Williamson's[14] vortex dislocations—our *vortex-adhesion mode*—and Williamson's[27] *A* and *B mode* with spanwise wavelengths of 4 and 1 diameters, respectively, are experimentally reproduced and for the first time numerically simulated. In Sec. IV C, the 3-D Floquet mode predicted by Noack, König, and Eckelmann[15] with a low-dimensional Galerkin method is identified as a separate 3-D instability. This instability has a spanwise wavelength of roughly two diameters and is called the *C mode* in the following. Thus, the three global shedding states, the A, B, and C mode, can easily be distinguished in terms of their characteristic spanwise wavelengths. A detailed comparison of their spatial structures is presented in Sec. IV D. In Sec. IV E, a control-wire technique for the suppression of three-dimensionality up to a Reynolds numbers of approximately 230 is presented. Finally (Sec. IV F), the interaction of the four instability processes is described.

A. Vortex-adhesion mode

The finite-difference computations can reproduce Williamson's[14] spot-like "vortex dislocations" for a sufficiently large domain size L (see Fig. 5). In this figure, the wavelength of the spanwise domain is $L/D=24$, which is one order of magnitude larger than in previous simulations.[9–12] The isopressure surface from the numerical data (Fig. 5, top) looks similar to the experimental hydrogen-bubble-wire visualizations (Fig. 5, bottom). Both structures identify essentially the primary von Kármán vortices. These vortices seem to "adhere" to slowly migrating points on the cylinder surface. Hence, we propose the term *vortex-adhesion mode* for this phenomenon. This mode is self-sustaining in the range $160<\mathrm{Re}<230$.

In the experiments, vortex-adhesion points originate at the ends of the cylinder as the Reynolds number is slightly increased above the critical value 160. At supercritical values $\mathrm{Re}>160$, these points occur intermittently along the whole cylinder span with a nearly uniform statistical distribution (see Fig. 6, bottom). The amount of adhesion points tends to increase with the Reynolds number. At $\mathrm{Re}<180$, the von Kármán vortices typically shed obliquely between two neighboring adhesion points. At $\mathrm{Re}\geqslant 180$, many regions between two neighboring adhesion points are often characterized by A-mode patterns with a few spanwise periods (see Sec. IV B). If the B mode (see Sec. IV B) dominates the vortex shedding at $\mathrm{Re}>230$, no pronounced adhesion points are observed. As the Reynolds number is slowly decreased below $\mathrm{Re}=160$, the adhesion mode is finally replaced by parallel or oblique shedding. Under suitable conditions, a self-sustaining adhesion mode is also experimentally obtained in the range $140<\mathrm{Re}<160$, for instance, when the Reynolds number is decreased sufficiently rapidly from irregular values, say $\mathrm{Re}=800$, to a subcritical value. Then, the shedding is characterized by one or a few adhesion points, which finally assume steady asymptotic positions, which are constant for the whole period of investigation, i.e., many thousand shedding periods (see Fig. 6, top).

The process of the creation and the propagation of the adhesion points suggests that the adhesion mode affects the vortex shedding in the range $160<\mathrm{Re}<230$ for arbitrarily large aspect ratios and any end condition in the post-transient state. In the present experiments, the vortex-adhesion mode is observed for four different setups with aspect ratios from

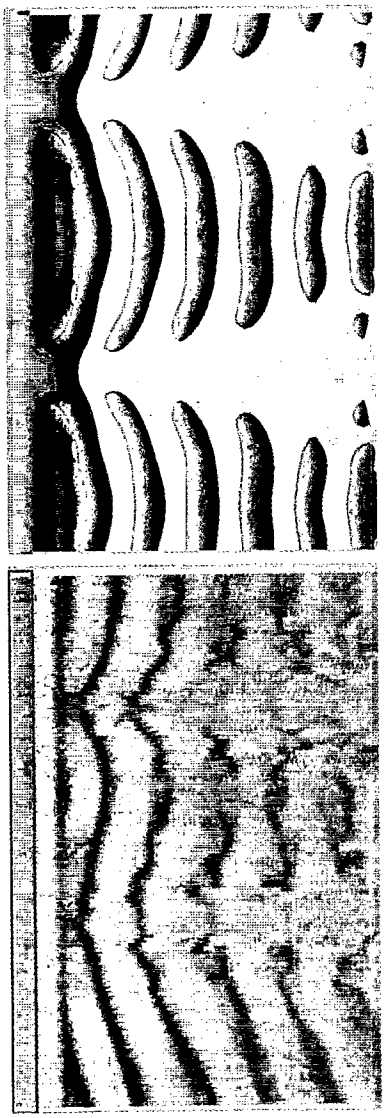

FIG. 5. Illustration of the vortex-adhesion mode from the numerical computation (top) and from the experimental flow visualization (bottom). The view section is given by $-0.5<x/D<16$, $0<z/D<24$. In both illustrations, the cylinder is situated at the left and the flow direction is from left to right. The numerically obtained vortex-adhesion mode (top) is described by an instantaneous isopressure surface $p=-0.2$ at Re=160. In the experiments (bottom), the wake structures at Re=161 are visualized with a hydrogen-bubble wire positioned at $(x_w/D;y_w/D)=(1.5;0)$. Thus, the hydrogen bubbles (dark regions) concentrate on both sides of the von Kármán vortex street. The aspect ratio of the cylinder is given by $L/D=93$. Similar structures are also obtained with a wire located far upstream $x_w/D\sim 50$ and far downstream (see Fig. 6).

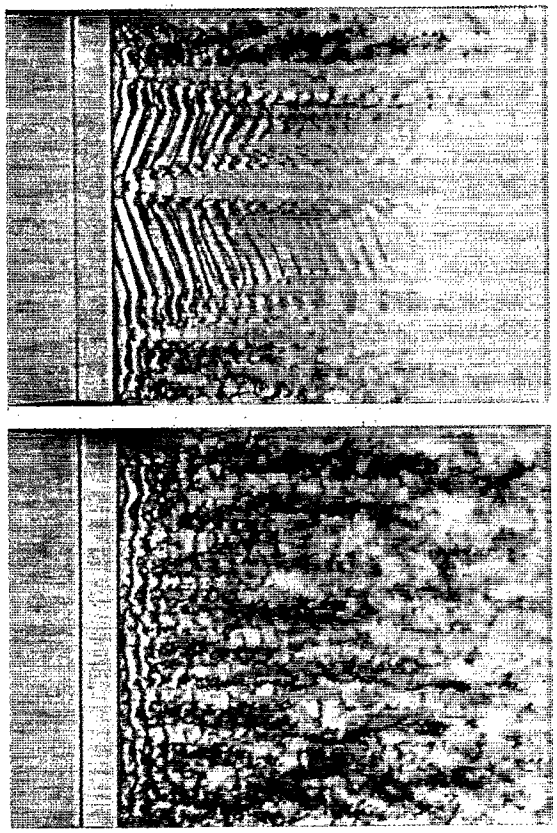

FIG. 6. Experimental flow visualization of the vortex-adhesion mode at a subcritical Reynolds number Re=152 (top) and at a supercritical value Re =176 (bottom). Each figure displays the cylinder (left), the two end plates (see the top and bottom side of the frame), and the hydrogen-bubble wire being fixed at the end plates (the beginning of a streak surface). The aspect ratio is given by $L/D=133$ and the wire is located at $(x_w/D;y_w/D)=(16;2)$.

50 to 133 and two kinds of end conditions (see Table V). Naturally, the transient time in which the adhesion points reach the midspan region increases with the aspect ratio. This situation is analogous to the transient "phase fronts" between parallel and oblique shedding in the regular Reynolds number range 50<Re<160. These phase fronts originate at the cylinder ends and move toward the midspan region with constant speed.[5,28] Finally, the whole span of the cylinder is governed by a chevron pattern or oblique shedding. Thus, even laminar shedding seems to be always affected by the end conditions for arbitrarily large aspect ratios.

In the numerical simulations, no end conditions are taken into account. Instead, a spanwise wavelength L is assumed. Hence, the adhesion points cannot be created in the same manner as in the experiments. In fact, the adhesion mode does not seem to occur naturally from a slightly three-dimensionally perturbed 2-D solution in the whole investigated Reynolds number range. Yet, the vortex-adhesion mode can be induced by inserting a strong localized spanwise inhomogeneity in the initial conditions provided that the chosen spanwise domain L is large enough. Once the vortex adhesion mode is "excited," it is found to be self-sustaining in the range 160<Re<230. Like in the experiments, the numerical simulations may yield adhesion points for lower Reynolds numbers 140<Re<160. While most of these adhesion points slowly decay, some of them seem to be self-sustaining—depending on the initial conditions. This behavior agrees with the experimental finding that the adhesion mode can only be induced under carefully controlled conditions for subcritical values Re<160.

Williamson's[5] experimental finding of a hard hysteretical onset of three-dimensionality is numerically reproduced. This hard transition can be inferred from the discontinuous behavior of the Strouhal number St, the mean drag coeffi-

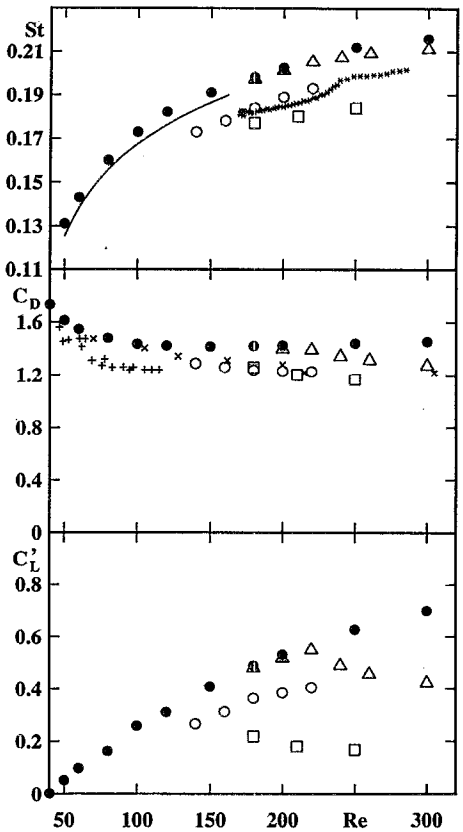

FIG. 7. The same as Fig. 3, but including numerical data for the hard vortex-adhesion transition (○), for the soft A-mode transition (△), for the soft C-mode transition (□), and empirical Strouhal data of König[39] for his oblique shedding mode $n=2$ merging into transitional vortex shedding (*).

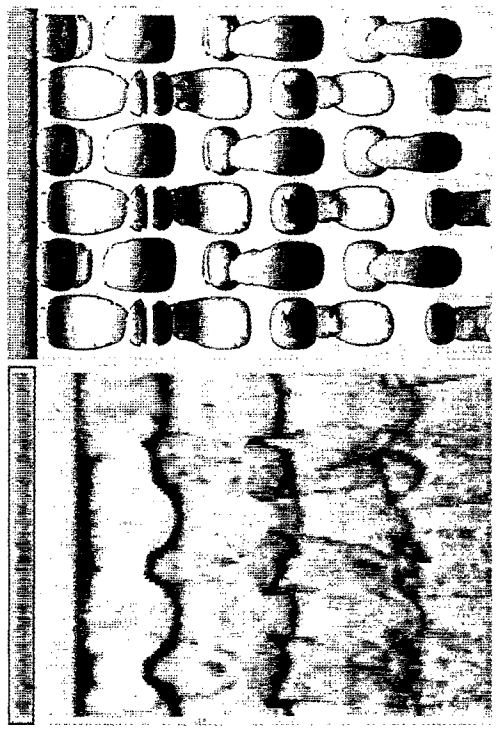

FIG. 8. Illustration of the A mode in the view section, $-0.5<x/D<16$, $0<z/D<12$. Top: isovorticity surface $\omega_x=0.02$ of the numerical solution at Re=200. Bottom: experimental flow visualization at Re=196. The aspect ratio is $L/D=93$. The hydrogen-bubble wire is located at $(x_w/D;y_w/D)=(2;1)$, i.e., only one side of the von Kármán vortex street is visualized.

cient C_D, and the RMS amplitude of the lift coefficient C'_L in terms of the Reynolds number (open circles in Fig. 7). The discontinuity can only be observed in the presence of the vortex-adhesion mode. Otherwise, the global flow quantities St, C_D, and C'_L depend continuously on the Reynolds number (open triangles in Fig. 7), like in previous numerical simulations of Karniadakis and Triantafyllou,[9] of Tombouldes, Triantafyllou, and Karniadakis,[10] and of Noack and Eckelmann.[11,12] In these simulations, the chosen spanwise wavelength L did not significantly exceed three diameters. In this case, possible adhesion points can be, at most, a distance L apart. Yet, our experiments and the simulations show that adhesion points annihilate each other when they are only a few diameters apart. Upon the annihilation, the von Kármán vortices reconnect from both sides of the adhesion point and shed nearly parallel from the cylinder. No hysteretical onset of three-dimensionality and no vortex adhesion has been numerically reproduced before because of the small spanwise domain sizes in the previous simulations.

Hence, the hard, jump-like cylinder–wake transition seems to be intimately connected with the existence of the vortex-adhesion mode. In the experiments, vortex-adhesion points are always induced by the end conditions for Re>160. Therefore, the hard *vortex-adhesion transition* appears to be the natural onset of three-dimensionality under experimental conditions, i.e., for cylinders with finite aspect ratio. In the simulations, the adhesion mode is also a self-sustaining shedding state, but it has to be excited by strong inhomogeneities in the initial conditions.

B. A and B mode

The finite-difference computations can also reproduce Williamson's experimental observation of two distinct spanwise patterns in the transitional Reynolds number range, his *A* and *B mode*. According to Williamson, the A mode "represents the inception of streamwise vortex loops, for Re =180 and above" with a spanwise wavelengths around three diameters, whereupon the B mode "represents the formation of finer-scale streamwise vortex pairs, for Re=230 and above," with a spanwise length scale around one diameter (see Fig. 2 in Ref. 14).

For the computations of the A and B mode, nearly 2-D initial conditions were employed. The simulations were carried out for various spanwise domain sizes L between 6 and 18 diam in order to guarantee that the simulated wake structures, including the spanwise wavelengths, depend insignificantly on the numerical boundary conditions.

In Fig. 8, the numerical solution and the experimental realization of the A mode is illustrated at Re=200. The mode displays a dominant spanwise wavelength of four diameters. Similarly, Williamson's B mode with a spanwise wavelength of one diameter can be experimentally and numerically reproduced at Re=250 (see Fig. 9). The hydrogen bubbles (Fig. 9, bottom) seem to concentrate in the primary von

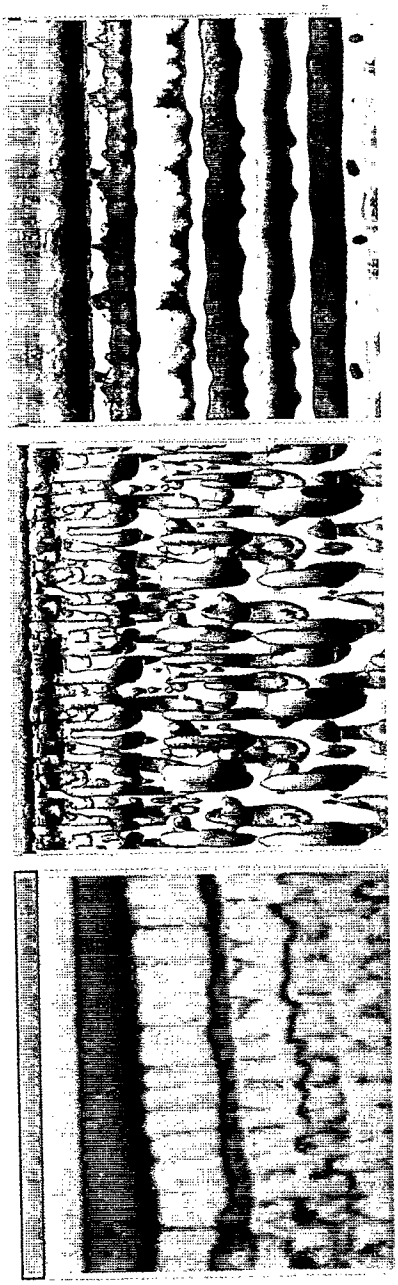

FIG. 9. Illustration of the B mode in the view section, $-0.5<x/D<16$, $0<z/D<18$. Top: isovorticity surface $\omega_z=\pm 0.50$ of the numerical solution at Re=250. Middle: isovorticity surface $\omega_x=0.15$ of the same solution. Note that the top and middle figures illustrate the *spanwise* and *streamwise* vorticity components, respectively. Bottom: experimental flow visualization at Re=254, the aspect ratio being $L/D=71$. The hydrogen-bubble wire is positioned at $(x_w/D;y_w/D)=(2;1)$, i.e., on one side of the von Kármán vortex street.

Kármán vortices and in the secondary vortices in the streamwise direction. The primary and secondary vortices are illustrated by numerically obtained isovorticity surfaces for the spanwise and streamwise component in Fig. 9 (top and middle, respectively). In the far wake, the secondary vortices have the tendency to merge in large-scale structures.

The spanwise structure in the near wake is displayed in Fig. 10 from simulations at different Reynolds numbers. For Re=200 and Re=240 (Fig. 10, top and bottom) the A and B

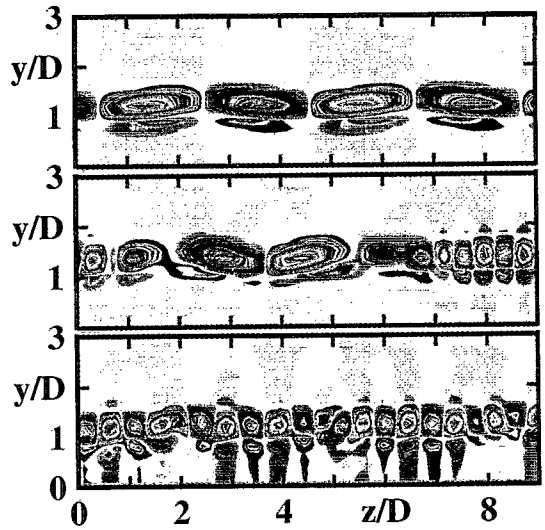

FIG. 10. Spanwise structure of the A and B mode. Instantaneous contour plots of the numerically obtained vorticity component ω_x in the plane $x/D=4$ at Re=200, 220, and 240 (top to bottom).

mode, respectively, can be numerically reproduced in a pure form, while at intermediate Reynolds numbers around Re =220, both modes generally coexist (Fig. 10, middle). Williamson[27] also observes a transition from the large-scale A-mode to a fine-scale B-mode pattern around Re=230. While Williamson's wavelength of $1D$ for the B mode is well confirmed, our numerical and experimental value of $4D$ for the A mode is somewhat larger. The value of approximately $4D$ is confirmed by a recent global stability analysis of Barkley and Henderson,[29] based on a highly accurate spectral method. The numerically obtained ω_x-contour diagram for the B mode (Fig. 10, bottom) is in good qualitative agreement with recent unpublished PIV experiments of Brede[30] for Re=400 and with the elaborate PIV study of Wu.[31]

The A mode occurs at Re>180 and gets gradually displaced by the B mode at Re>230. The characteristic B-mode wavelength of roughly $1D$ can be experimentally and numerically observed up to at least Re=1000. Without vortex adhesion, the *A-mode transition* from 2-D shedding to the 3-D wake is smooth, i.e., the global flow quantities St, C_D, and C_L' depend continuously on the Reynolds number with a small kink at the onset of three-dimensionality (open triangles in Fig. 7). In the computations, vortex adhesion at the cylinder can be avoided by employing suitable 2-D initial conditions superimposed by a small 3-D perturbation, which is periodic in the spanwise direction. In the experiments, localized vortex deformations are generally introduced by the end conditions, and can be avoided by placing a thin control wire in the near wake or by employing other control mechanisms.

C. C mode

In addition to the A and B mode, a different kind three-dimensionality can be observed, called the *C mode* in the following. This mode displays a spanwise periodicity with a

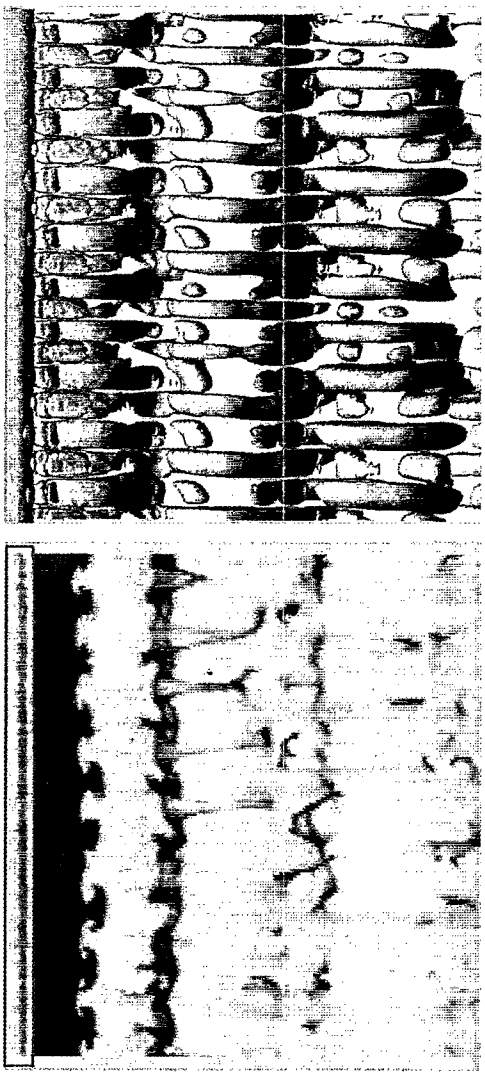

FIG. 11. Illustration of the C mode in the view section, $-0.5<x/D<16$, $0<z/D<18$. Top: isovorticity surface $\omega_x=0.05$ of the numerical solution at Re=210. The thin wire is placed at $(x_w/D;y_w/D)=(0.75;0.75)$. Bottom: experimental flow visualization at Re=215. The setup is the same as in Fig. 5, except for an aspect ratio of $L/D=71$ and a visualization wire located at $(x_w/D;y_w/D)=(0.75;0.75)$.

wavelength of roughly $2D$. It can be seen in flow visualizations for 170<Re<270 (see Fig. 11, bottom) when a thin wire of diam $0.006D$ is placed parallel to the cylinder axis in a narrow region including the locations $(x_w/D;y_w/D)=(0;0.90)$ and $(x_w/D;y_w/D)=(0.75;0.75)$.[21] Of course, the wire may also be placed symmetrically on the other side of the plane $y=0$. Possibly, the wire suppresses the vortex adhesion and the A mode and impairs the B mode at 230<Re<270. Thus, the C mode can grow without being replaced by the other 3D modes. In the present publication, no physical mechanism for the effect of the wire can be presented.

The effect of the wire can be simulated in the finite-difference computation by setting the velocity zero on a grid line $(x/D;y/D)=(0.75;0.75)$. The effective thickness of the wire is of the order of the grid size, i.e., $\sim 0.05D$. In this case, also the numerical simulations yield a 3-D spanwise pattern with a wavelength of approximately $1.8D$ (see Fig. 11, top, and Fig. 12), i.e., reproduce the C mode. Experiments (see Fig. 45 of Ref. 21) and numerical computations (open squares in Fig. 7) yield that the C mode significantly decreases the Strouhal number, as compared to 2-D shedding. This difference is larger than the corresponding frequency drop in the A-mode transition (open triangles in Fig. 7). For Re>200, the shedding frequency is even smaller than for the vortex-adhesion mode (open circles in Fig. 7). In addition, the effect of the C mode on the lift amplitude and mean drag is large compared with the A, B, and vortex-adhesion modes. Thus, all four kinds of 3-D shedding modes *reduce* the St, C_D, and C_L' values, as compared to the corresponding 2-D simulation. Mittal and Balachandar[32] confirm and explain this tendency for the lift and drag of the B mode in the irregular range.

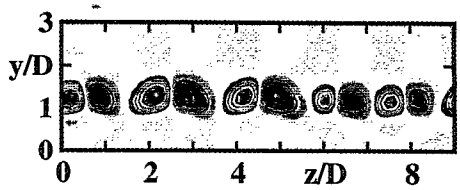

FIG. 12. Spanwise structure of the C mode. Instantaneous contour plot of the vorticity component ω_x in the plane $x/D=7.5$ from the numerical simulation of Fig. 11.

In Fig. 13, experimental values of spanwise wavelengths are displayed in terms of the Reynolds number for different experimental setups. The values are seen to be discretely grouped around one, two, and four diameters. Hence, the C-mode instability appears to be distinct from the A and B mode.

The experimental setup with the control wire leads to a smooth *C-mode transition* with a 3-D periodic flow for 170<Re<200 and a quasiperiodicity with a low-frequency component for 200<Re<270. At Re>270, the flow becomes irregular (see Fig. 14). This behavior agrees well with the transition scenario predicted by the low-dimensional Galerkin model of Noack[33] and Noack and Eckelmann,[11,12] includ-

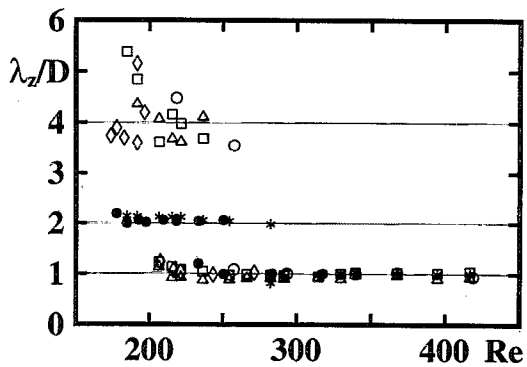

FIG. 13. Experimental spanwise wavelengths λ_z in terms of the Reynolds number for various experimental setups: (○): aspect ratio $L/D=71$, thin wire at $(x_w/D;y_w/D)=(-1.04;0.10)$; (□): $L/D=71$, $(x_w/D;y_w/D)=(0;1.05)$; (△): $L/D=71$, $(x_w/D;y_w/D)=(0.53;0.91)$; (*): $L/D=71$, $(x_w/D;y_w/D)=(0.75;0.75)$; (●): $L/D=50$, $(x_w/D;y_w/D)=(0;0.90)$; and (◇): $L/D=93$, without wire.

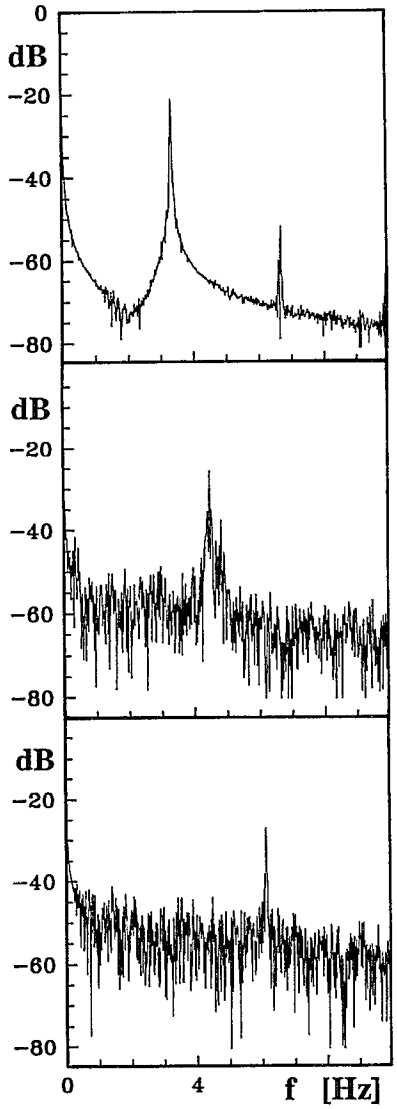

FIG. 14. Experimental power spectra of the C-mode transition at Re=177, 233, and 317 (top to bottom). The cylinder diameter is 3 mm. The thin wire is placed at $(x_w/D;y_w/D)=(0;0.9)$. Thus, a dominant spanwise wavelength of $2D$ is obtained (see the solid circles in Fig. 13). The spectra are obtained from hot-film signals at $(x/D;y/D)=(8.7;1.5)$.

ing the predicted wavelength of $1.8D$ and the critical Reynolds numbers of 170, 200, and 280 for three-dimensionality, quasiperiodicity, and irregularity, respectively. The quasiperiodicity in the experimental velocity fluctuation (Fig. 14, middle) is superimposed by some background noise, which is not present in the Galerkin results.

The most unstable 3-D Floquet mode and the asymptotic solution of the Galerkin model display two oppositely oriented vortex rolls alternatingly on the upper and on the lower shear layer in the near wake (see Ref. 3). These vortex rolls can also be seen in the ω_x vorticity distribution of the more accurate finite-difference simulations (Fig. 12). Hence, the low-dimensional Galerkin model appears to describe the transition scenario via the C mode. The wake resolution of this model seems to be too coarse for the simulation of the A and B mode. In particular, the azimuthal resolution with a modified trigonometric system up to only fourth order appears to be too small.

In the Galerkin model, the C mode evolves naturally as the most amplified 3-D perturbation without an imposed wake asymmetry or other control mechanisms. In the experiments, the C mode is excited by an asymmetric location of the control wire. In order to elucidate the role of this asymmetry, a symmetric setup with two wires at $(x_{1,2}/D;y_{1,2}/D)=(0.75;\pm 0.75)$ is numerically investigated. For this case, spanwise vortices with a slightly larger wavelength of $2.2D$ are observed. The slight increase of the wavelength may result from the larger effective cylinder diam due to the displacement effect of both wires. Thus, the C mode for an effectively larger cylinder is obtained. The C-mode structure with a spanwise wavelength of two diameters is also numerically obtained at Re=200 when the cylinder performs a transversal oscillation with a small amplitude and a frequency corresponding to half the natural shedding frequency. Thus, the C mode is numerically observed for two different symmetric control processes. Hence, the occurrence of the C mode is not intimately connected to asymmetric excitation.

D. Comparison of the A, B, and C mode

The vortex-adhesion mode can easily be distinguished from the A, B, and C modes. The adhesion mode represents a *local* deformation of the *primary* von Kármán vortices, whereupon the A, B, and C modes are associated with *global, secondary* vortices on the von Kármán vortices. These three secondary vortices are characterized by different spanwise wavelengths, but have a similar spatial structure (see Fig. 10 and Fig. 12). In this section, the A-, B-, and C-mode structures are compared in detail.

Figure 15 displays the ω_y vorticity component of the A-, B-, and C-mode shedding in the centerplane $y=0$. The spanwise wavelength of the A and C mode are seen to characterize the near and far wake. In contrast, the B-mode pattern governs only the near wake. In the far wake, the one diameter vortices seem to merge into larger-scale structures. The ω_y vorticity component of the A mode is nearly uniformly distributed in the downstream direction. In contrast, the secondary vortices of the C mode appear to concentrate in regions that are roughly one wavelength of the von Kármán vortex street apart. Similarly, the B-mode vortices intersect the centerplane near the lines $x/D=2$, 4, and 6. Clearly, the "footprints" of the A-, B-, and C-mode vortices in the plane $y=0$ are distinct—apart from the wavelength. Recent PIV experiments,[30] and our simulations[20] reveal that the primary von Kármán vortices are deformed by the secondary A-mode vortices to a noticeable extent. In contrast, the von Kármán vortices are hardly deformed by the presence of the B and C mode. Thus, Williamson[14] concludes from his flow visualizations that the A-mode pattern is caused by a deformation of the primary vortices, whereupon the B-mode structure is due to secondary streamwise vortices. Yet, it must be emphasized that also the A mode is associated with secondary vortices. This is experimentally confirmed by Fey.[21]

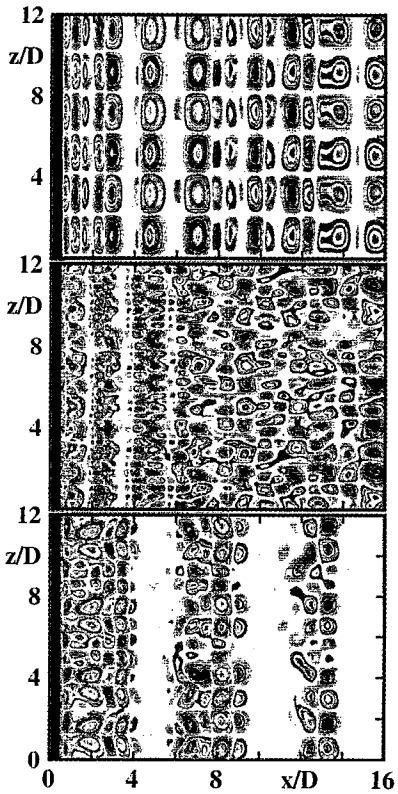

FIG. 15. Secondary vortices of the A, B, and C modes (top to bottom). Instantaneous contour plots of the numerically obtained vorticity component ω_y in the x,z plane at Re=200, 240, and 210 (top to bottom). The numerical solutions for A, B, and C modes are the same as in Figs. 8, 9, and 11.

The primary von Kármán vortices of A-, B-, and C-mode shedding are illustrated in Fig. 16. The geometry of the vortex street for the A and B mode are very similar. In contrast, the C-mode shedding is associated with increased downstream wavelength λ_x of the von Kármán vortices. This increased λ_x value induces a noticeably reduced shedding frequency, discussed in Sec. IV C. In addition, a pairing mechanism of the von Kármán vortices can be seen. The vortex pairing has also been observed in the C-mode excitation by a transversal cylinder oscillation (see Sec. IV C). Hence, the secondary vortices of the C mode appear to be intimately linked with the vortex pairing of the primary von Kármán vortices.

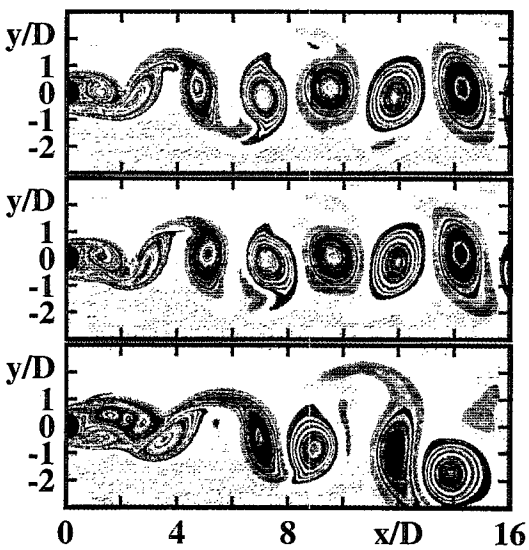

FIG. 16. Primary von Kármán vortices in the presence of the A, B, and C mode (top to bottom). Contour plots of the numerically obtained vorticity component ω_z in the x,y plane for the same instantaneous velocity fields as in Fig. 15.

TABLE VI. Properties and effects of the A, B, and C modes, based on the numerical results.

	A mode	B mode	C mode
Re range	180–230	200<Re	170–270
Spanwise wavelength	$\lambda_z/D\approx 4$	$\lambda_z/D\approx 1$	$\lambda_z/D\approx 2$
Secondary vortices	Near and far wake	Near wake only	Near and far wake
von Kármán vortex axes	Slightly deformed (4D wavelength)	Nearly parallel	Nearly parallel
von Kármán vortex spacing	Nearly equidistant	Nearly equidistant	Pairing in x direction

In case of the oscillating cylinder, the vortex pairing is accompanied by a period doubling in the frequency domain. This period doubling is externally forced by a subharmonic excitation. Interestingly, a period doubling is also observed for a Reynolds number of Re≈270 in the Galerkin model of Noack and Eckelmann.[3] The numerical simulation of Karniadakis and Triantafyllou[9] also yields a period doubling mechanism below Re=300. They chose a spanwise domain size of $L/D=1.57$, which is slightly below the C-mode wavelength of $\lambda_z/D=1.8$. The spanwise length scale of their near and far wake structures coincide with the domain size. Hence, their flow features appear to have more in common with the C mode than with the A or B mode.

The simulated control wire induces a noticeable asymmetry in the vortex shedding (Fig. 16, bottom). Yet, it should be noted that the C-mode shedding is also observed in our experiments, in which the ratio between the control wire and the cylinder diam is one order of magnitude smaller and therefore the asymmetry of the boundary conditions much less pronounced. Table VI summarizes some similarities and differences of the A, B, and C modes.

E. Suppression of three-dimensionality

The visualization wire placed parallel to the cylinder axis may also be used to suppress *all four* 3-D instability modes in a part of the transitional Reynolds number range (for details see Ref. 21). Placing the wire at $(x_w/D;y_w/D)=(1.05;0)$, the experimental flow visualization yields nearly 2-D periodic shedding at Re<230 (Fig. 17, bottom). In the numerical computation, 3-D fluctuations are found to decay at Re<250, when the wire is simulated at the same location, i.e., the stable post-transient solution represents parallel shedding (Fig. 17, top). The discrepancy for the experimentally and numerically observed onset of three-dimensionality at Re=230 and 250, respectively, may be attributed to the larger effective thickness of the numerical

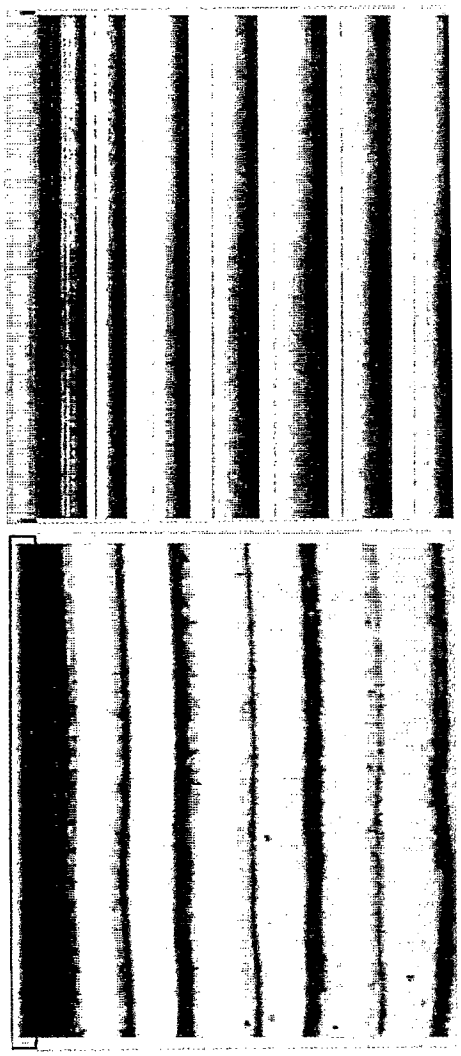

FIG. 17. Illustration of the suppressed onset of three-dimensionality in the view section, $-0.5<x/D<16$, $0<z/D<18$. Top: isopressure surface $p=-0.2$ of the numerical solution at Re=220. The thin wire is placed at $(x_w/D;y_w/D)=(1.05;0)$. Bottom: experimental flow visualization at Re=219. The same setup as in Fig. 5 is employed, the aspect ratio being $L/D=71$. The visualization wire is also located at $(x_w/D;y_w/D)=(1.05;0)$.

wire as compared to the experimental one. The effective suppression of 3-D fluctuations by the wire can also be seen in the Fourier spectra of the experimental velocity fluctuations (Fig. 18). In the range 240<Re<270, the A-, B-, and vortex-adhesion mode occur intermittently. At Re>270, the wire is found to have little influence on the wake dynamics anymore, and the spanwise wake pattern is dominated by the B mode.

The employed control-wire technique has been successfully applied by Strykowski and Sreenivasan to delay the onset of periodic vortex shedding[34] and to control the boundary-layer transition.[35] Interestingly, the control-wire positions, for which vortex shedding is effectively retarded, is similar to our experimentally determined region in which the A and B mode is suppressed, i.e., the C mode is excited. In Ref. 35, the authors emphasize that small vibrations of the control wire may drastically affect the flow. In our experiments, the wire displays hardly noticeable vibrations when it is located in the vicinity of $(x_w/D;y_w/D)\approx(1,0)$. Yet, the independent confirmation of our experimental results with a simulated stationary control-wire setup clearly shows that the retarded onset of three-dimensionality is not an artifact of these wire vibrations. For the C-mode setup (Sec. IV C) and vortex-adhesion setup (Sec. IV A), the wire did not vibrate within the experimental resolution.

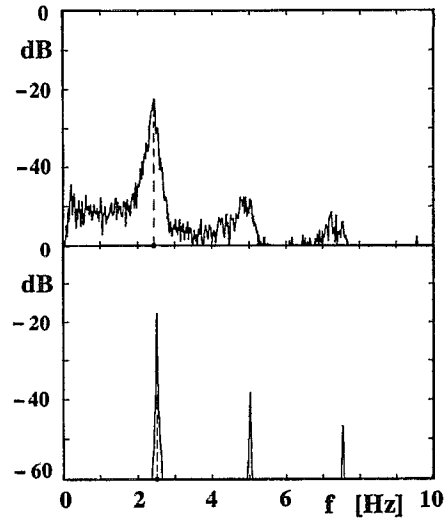

FIG. 18. Experimental power spectra at Re=219 without (top) and with (bottom) a wire at $(x_w/D;y_w/D)=(1.05;0)$. The cylinder diameter is 4 mm. The aspect ratio is $L/D=71$. The spectra are obtained from hot-film signals at $(x/D;y/D)=(6.0;1.5)$.

F. Interaction of the 3-D modes

Figure 19 summarizes the Reynolds number intervals in which the vortex adhesion, and the A, B, and C modes can be observed. All four modes can be obtained in "pure" states along the whole cylinder span, under the conditions specified in the previous sections. In these shedding states, no noticeable contributions of the remaining modes are evident. Yet, there exist several overlap intervals in which these modes interact. For instance, spanwise A- and B-mode cells, each consisting of several wavelengths, generally coexist in a small Reynolds number interval around 230 according to the simulation. In the experiments, this coexistence appears at

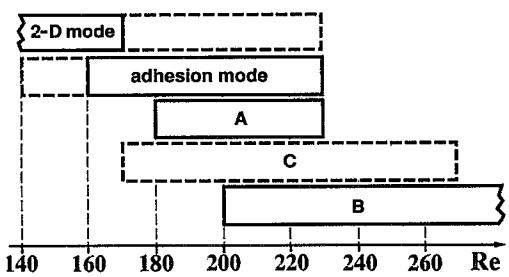

FIG. 19. Observed shedding modes and their Reynolds number ranges. The modes are displayed in solid (dashed) boxes, when they are self-sustaining (can easily be excited under suitable conditions). For details, see the text.

slightly smaller Reynolds numbers around 220. For Re<230, also vortex-adhesion points perturb a neighboring spanwise region. This region is characterized by large shedding angles of the von Kármán vortices and by irregular spanwise wiggles. The vortex-adhesion points tend to retard the shedding of the von Kármán vortices, i.e., the shedding frequency is reduced along the whole cylinder span. In the presence of vortex-adhesion points, the power spectra of the experimental velocity fluctuations display no peaks at a larger frequency corresponding to the theoretically obtained pure A mode. For suitable control-wire positions (see Sec. IV C), C-mode structures without significant A-mode or B-mode contributions may be observed in the range 170<Re<270. For Re>230, B-mode patterns with wavelengths of one diameter may occur intermittently in the experiments.

The above phenomenology suggests that all four modes arise from local or global 3-D instabilities of the 2-D periodic vortex shedding. The end conditions serve as a finite nonvanishing perturbation for the excitation of the vortex-adhesion mode, but the end conditions seem unnecessary to sustain any of the above shedding states. This conclusion is confirmed by the fact that all 3-D modes can be numerically computed, assuming a periodicity in the spanwise direction and without taking end effects into account. The A, B, and C modes appear to result from unstable infinitesimal perturbations, while the vortex-adhesion mode must be excited by a finite perturbation. This hypothesis would explain why the A-mode and C-mode scenario display a soft onset of three-dimensionality, while the vortex-adhesion mode scenario is characterized by a hard hysteretical transition.

V. CONCLUSIONS

Williamson's[27,14] experimental observation of three different 3-D shedding modes in the transitional cylinder wake is numerically reproduced for the first time. These modes include the vortex-adhesion mode characterized by spot-like vortex deformations, a large-scale A-mode pattern in the range 180<Re<230 with a spanwise wavelength around four diameters, and a fine-scale B-mode structure in the range 230<Re. In the simulation, periodic spanwise boundary conditions are assumed, i.e., the cylinder is effectively infinitely long. Experimentally, these phenomena are observed for different aspect ratios and other end conditions, as employed by Williamson. Thus, all three shedding modes seem to be able to exist as stable states independently of the end conditions. In particular, the vortex-adhesion mode is identified as a self-sustaining shedding state. Hence, the 3-D modes are likely to arise from instability processes under nominally 2-D boundary conditions.

The theoretically predicted 3-D Floquet mode originating at Re=170 with a spanwise wavelength of 1.8 diameters (Noack, König, and Eckelmann;[15] Noack and Eckelmann[3]) is shown to be a separate instability process, called a C mode in this publication. For the first time, this C mode and the resulting spanwise structure is reproduced in the experiments and an accurate numerical simulation, placing a thin wire at suitable locations in the near wake. Experiments indicate a 3-D wake structure with a dominant spanwise wavelength of roughly two diameters in the range 170<Re<270.

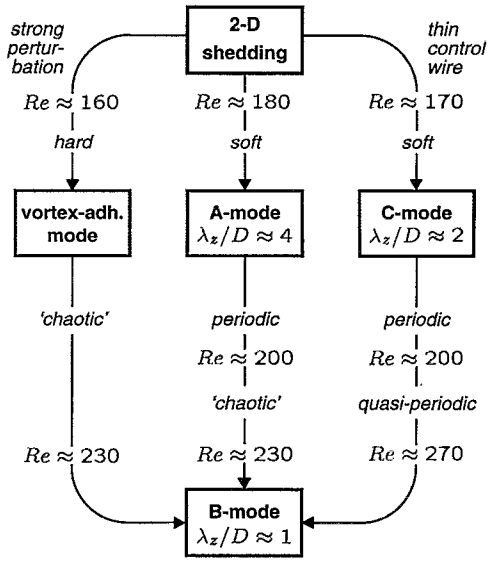

FIG. 20. Simplified sketch of the observed transition scenarios: the vortex-adhesion transition (left branch), the A-mode transition (middle branch), and the C-mode transition (right branch). The retarded onset of three-dimensionality, i.e., the direct transition from 2-D shedding to the B mode at Re≈230, is not included in this figure. For details, see the text.

Our present numerical and experimental results for the transitional Reynolds number range do not suggest the existence of further distinct localized or global 3-D shedding modes occurring naturally or under small perturbations. Even a variety of experimentally and numerically realized stationary and periodic control processes do not give rise to three-dimensional structures, which cannot be identified as one of the four 3-D shedding modes. For instance, the acoustically induced "netting pattern" at Re=143 (Fig. 9 in Ref. 36) appears to be an excited A mode.

Our simulation and experiment yield four different kinds of transition scenarios: a hard vortex-adhesion, a soft A mode, a controlled C-mode, and a retarded transition (see Fig. 20). The vortex-adhesion transition with a hard hysteretical onset of three-dimensionality can be induced numerically by finite localized perturbations in the initial conditions, provided that the spanwise domain is large enough. This hard transition appears to be common in the experiments, where end effects always give rise to finite localized 3-D perturbations, which originate at the cylinder ends, and are finally distributed along the whole cylinder span. The A-mode transition with a continuous onset of three-dimensionality can be numerically obtained with nearly 2-D initial conditions. Both the irregular vortex-adhesion mode and the time-periodic A mode can be considered as stable coexisting Navier–Stokes attractors roughly in the range 170 <Re<230. The soft C-mode transition, predicted by the low-dimensional Galerkin model of Noack and Eckelmann,[11,12] can be numerically and experimentally observed when a thin wire is located in the near wake. Naturally, this is a controlled transition; the C mode appears to be too "weak" in order to compete with the A and B mode under natural conditions. In the Galerkin model, the A and B modes seem to be "suppressed" by a rather low azimuthal resolution. Fi-

nally, a retarded transition at Re=230 can be observed from parallel shedding to the B mode by placing a control wire in the centerplane closely behind the cylinder. This suppression of three-dimensionality with a control-wire technique is an analog of a similar procedure of Strykowski and Sreenivasan,[34] who suppress the onset of 2-D vortex shedding.

Summarizing, most present controversies on the cylinder–wake transition can easily be explained in the framework of the A, B, C, and vortex-adhesion modes. This clarification includes the origin of three different spanwise wavelengths of roughly one, two, and four diameters in the literature and the role of the vortex-adhesion mode in the discrepancy between the experimentally observed hard and the numerically obtained soft transition. The slow irregular dynamics of the vortex-adhesion points appears also to be responsible for the lacking experimental confirmation of the numerically predicted 3-D time-periodic flow. The described phenomenological aspects of the cylinder–wake transition are believed to be of importance for many bluff-body wakes. Yet, no physical mechanisms for the four distinct 3-D instabilities are proposed in the present publication. Research results on the physical origin of the A, B, C, and adhesion mode are the subject of a forthcoming publication.

ACKNOWLEDGMENTS

Two of the authors appreciate the support of the Alexander von Humboldt Stiftung (H.-Q. Z.) and the Deutsche Forschungsgemeinschaft Ec41/12-2 (M. K.). We thank H. Vollmers for supporting us with his excellent visualization software "comadi" for our numerical data. We are indebted to the rest of our former wake team at the meanwhile disintegrated fluid-dynamics department of the Max-Planck-Institut. In particular, we thank M. Brede and J. Wu for providing us with their most recent PIV results on the spanwise structures of the cylinder wake. We are grateful to the referees for making many valuable suggestions that initiated some further interesting research results and that contributed to a more comprehensive presentation.

[1]K. R. Sreenivasan, P. J. Strykowski, and D. J. Olinger, "Hopf bifurcation, Landau equation, and vortex shedding behind circular cylinders," in *Forum on Unsteady Flow Separation*, edited by K. N. Ghia (American Society for Mechanical Engineers, Fluids Engineering Division, New York, 1987), Vol. 52, p. 1.

[2]M. Provansal, C. Mathis, and L. Boyer, "Bénard–von Kármán instability: Transient and forced regimes," J. Fluid Mech. **182**, 1 (1987).

[3]B. R. Noack and H. Eckelmann, "A global stability analysis of the steady and periodic cylinder wake," J. Fluid Mech. **270**, 297 (1994).

[4]C. H. K. Williamson, "Defining a universal and continuous Strouhal–Reynolds number relationship for the laminar vortex shedding of a circular cylinder," Phys. Fluids **31**, 2742 (1988).

[5]C. H. K. Williamson, "Oblique and parallel modes of vortex shedding in the wake of a circular cylinder at low Reynolds numbers," J. Fluid Mech. **206**, 579 (1989).

[6]C. H. K. Williamson and A. Roshko, "Measurements of base pressure in the wake of a cylinder at low Reynolds numbers," Z. Flugwiss. Weltraumforsch. **14**, 38 (1990).

[7]M. König, B. R. Noack, and H. Eckelmann, "Discrete shedding modes in the von Kármán vortex street," Phys. Fluids A **5**, 1846 (1993).

[8]M. Brede, H. Eckelmann, M. König, and B. R. Noack, "On discrete shedding modes of the cylinder wake in a jet with a homogeneous core," Phys. Fluids **6**, 2711 (1994).

[9]G. E. Karniadakis and G. S. Triantafyllou, "Three-dimensional dynamics and transition to turbulence in the wake of bluff bodies," J. Fluid Mech. **238**, 1 (1992).

[10]A. G. Tomboulides, G. S. Triantafyllou, and G. E. Karniadakis, "A mechanism of period doubling in free shear flows," Phys. Fluids A **4**, 1329 (1992).

[11]B. R. Noack and H. Eckelmann, "A low-dimensional Galerkin method for the three-dimensional flow around a circular cylinder," Phys. Fluids **6**, 124 (1994).

[12]B. R. Noack and H. Eckelmann, "Theoretical investigation of the bifurcations and the turbulence attractor of the cylinder wake," Z. Angew. Math. Mech. **74**, T396 (1994).

[13]F. R. Hama, "Three-dimensional vortex pattern behind a circular cylinder," J. Aerosp. Sci. **24**, 156 (1957).

[14]C. H. K. Williamson, "The natural and forced formation of spot-like 'vortex dislocations' in the transition of a wake," J. Fluid Mech. **243**, 393 (1992).

[15]B. R. Noack, M. König, and H. Eckelmann, "Three-dimensional stability analysis of the periodic flow around a circular cylinder," Phys. Fluids A **5**, 1279 (1993).

[16]J. Wu, J. Sheridan, J. Soria, and M. C. Welsh, "An experimental investigation of streamwise vortices in the wake of a bluff body," J. Fluid Struct. **8**, 621 (1994).

[17]J. H. Gerrard, "The three-dimensional structure of the wake of a circular cylinder," J. Fluid Mech. **25**, 143 (1966).

[18]S. Bloor, "The transition of turbulence in the wake of a circular cylinder," J. Fluid Mech. **19**, 290 (1964).

[19]C. H. K. Williamson and A. Prasad, "A new mechanism for oblique wave resonance in the 'natural' far wake," J. Fluid Mech. **256**, 269 (1993).

[20]H.-Q. Zhang, B. R. Noack, and H. Eckelmann, "Numerical computation of the 3-D cylinder wake," Max-Planck-Institut für Strömungsforschung Report No. 3/1994, Göttingen, 1994.

[21]U. Fey, "Aufbau einer Versuchsanlage zur Strömungssichtbarmachung und experimentelle Untersuchung der Nachlauftransition beim Kreiszylinder," Diplom thesis, Institut für Angewandte Mechanik und Strömungsphysik der Georg-August-Universtität, Göttingen, 1994.

[22]J. F. Thompson, F. C. Thames, J. K. Hodge, S. P. Shanks, R. N. Reddy, and C. W. Mastin, "Solutions of the Navier–Stokes equations in various flow regimes on fields containing any number of arbitrary bodies using boundary-fitted coordinate systems," in *Proceedings of the 5th International Conference on Numerical Methods in Fluid Dynamics*, edited by A. I. van de Vooren and P. J. Zandbergen, Lecture Notes in Physics (Springer-Verlag, Berlin, 1976), Vol. 59, pp. 421–427.

[23]G. E. Karniadakis and G. S. Triantafyllou, "Frequency selection and asymptotic states in the laminar wake," J. Fluid Mech. **189**, 441 (1989).

[24]C. A. J. Fletcher, *Computational Techniques for Fluid Dynamics; Volume II: Specific Techniques for Different Flow Categories* (Springer-Verlag, Berlin, 1988).

[25]H.-Q. Zhang and W. Shu, "Numerical simulations of vortex merging and vortex splitting in mixing layers," Sci. China A **33**, 686 (1990).

[26]H. Eisenlohr and H. Eckelmann, "Vortex splitting and its consequences in the vortex street wake of cylinders at low Reynolds numbers," Phys. Fluids A **1**, 189 (1989).

[27]C. H. K. Williamson, "The existence of two stages in the transition to three-dimensionality of a cylinder wake," Phys. Fluids **31**, 3165 (1988).

[28]P. Albarède and P. A. Monkewitz. "A model for the formation of oblique shedding patterns and 'chevrons' in cylinder wakes," Phys. Fluids A **4**, 744 (1992).

[29]D. Barkley (private communication, 1994).

[30]M. Brede (private communication, 1994).

[31]J. Wu, "Three-dimensional vortical structures in the wake of a bluff body," Ph. D. thesis (in preparation), Department of Mechanical Engineering, Monash University, 1994.

[32]R. Mittal and S. Balachandar, "Effect of three-dimensionality on the lift and drag of circular cylinders," TAM Report No. 774, Department of Theoretical and Applied Mechanics, University of Illinois at Urbana—Champaign, Urbana, Illinois 1994.

[33]B. R. Noack, "Theoretische Untersuchung der Zylinderumströmung mit einem niedrigdimensionalen Galerkin–Verfahren," Max-Planck-Institut für Strömungsforschung Report No. 25/1992, Göttingen, 1992.

[34]P. J. Strykowski and K. R. Sreenivasan, "On the formation and suppression of vortex 'shedding' at low Reynolds numbers," J. Fluid Mech. **218**, 71 (1990).
[35]P. J. Strykowski and K. R. Sreenivasan, "The control of transitional flows," *AIAA Shear Flow Control Conference*, 1985 12–14 March, Boulder, Colorado; also see Paper No. AIAA-85-0559.
[36]E. Detemple-Laake and H. Eckelmann, "Phenomenology of Kármán vortex streets in oscillatory flow," Exp. Fluids **7**, 217 (1989).
[37]D. J. Tritton, "Experiments on the flow past a circular cylinder at low Reynolds numbers," J. Fluid Mech. **6**, 547 (1959).
[38]C. Wieselsberger, "Über den Flüssigkeits- und Luftwiderstand," Phys. Z. **22**, 321 (1921).
[39]M. König, "Experimentelle Untersuchung des dreidimensionalen Nachlaufs zylindrischer Körper bei kleinen Reynoldszahlen," Mitteilungen aus dem Max-Plank-Institut für Strömungsforschung, No. 111, Göttingen, 1993.